

# BRO-JEPA: Learning Modular Arithmetic in Latent Space

Divyansh Jha<sup>\*,1,2</sup> Yuanfang Xie<sup>1</sup> Varan Mehra<sup>1</sup> Brennen Yu<sup>1</sup>

{djha32, yxie418, vmehra33, brennen.yu}@gatech.edu

<sup>1</sup>Georgia Institute of Technology

<sup>2</sup>NYU Langone Health

## Abstract

*Can neural networks learn abstract algebraic rules, or do they merely memorize training patterns? We investigate this using MNIST digits as states and modular arithmetic operations as actions in a JEPA-style latent world model. Standard supervised baselines and JEPA models with additive operation embeddings fit seen operations but fail to extrapolate reliably to unseen ones. To bridge this gap, we introduce a block-rotation predictor that imposes the circular structure of modulo-10 arithmetic in latent space. This enables strong zero-shot generalization, with the best ResNet-based JEPA block-rotation model achieving 99.46% zero-shot and 99.46% rollout accuracy. Our results suggest that latent world models can learn symbolic transformation rules when architecture matches the structure of the problem. Our code can be [accessed here](#).*

## 1. Introduction

Mathematical and logic reasoning are regarded crucial steps in building intelligent machines[12]. Current deep learning models have shown notable success in mathematical problems ranging from word problem solving to automated theorem proving. However, it remains unclear whether these models truly possess numeric reasoning capabilities, as they often fail to extrapolate beyond the numerical ranges or operations seen during training [13, 12]. This limitation suggests that many models may rely more on the statistic correlations in the training data rather than learning underlying arithmetic rules.

In deep learning, arithmetic is typically framed as a supervised prediction problem: given an input and an operation, the model predicts the resulting output. To better support mathematical operations, special neural arithmetic modules such as NALU and NAU introduce inductive biases for operations including addition, subtraction, multiplication, and division [13, 7]. Although these special struc-

tures improve arithmetic learning through built-in structural priors, they still suffer from robustness and generalization [8].

Recently, world models have demonstrated great potential in advanced machine intelligence [2, 9]. By learning abstract semantic representation and modeling dynamics directly in the compact latent space, world models provide efficient architecture for machine understanding, prediction, and planning [2]. Such learning and controlling in the latent space offers a natural framework for mathematical reasoning where mathematical rules can be represented as a structural transformation within the semantically meaningful latent space.

In this work, we build on the Joint Embedding Predictive Architecture (JEPA) [1]. Unlike traditional approaches that predict raw outputs, JEPA focuses on modeling transformations in the latent space. While JEPA-based approaches have shown strong performance in continuous settings involving deterministic spatial or temporal transformations, their effect on symbolic, axiomatic transformations remains largely unexplored.

We used JEPA training framework on the MNIST dataset [4]. The model receives an image of a number (the context image), along with a mathematical operation (the action, such as "+3"), and predicts the representation of the resulting number (the target). A context encoder extracts the representation from the context images. A predictor then takes this representation, applies the action, and predicts the representation of the correct answer. The model is trained by making the predicted representations and target representations as close as possible.

In addition to the standard neural network predictor commonly used in JEPA models, we also introduced a novel block-rotation predictor that enables strong zero-shot generalization in modular arithmetic tasks. We refer to this framework as BRO-JEPA. By incorporating inductive biases aligned with the cyclic structure of modulo arithmetic, BRO-JEPA organizes latent representations into a structured geometric manifold, enabling efficient learning with a relatively simple predictor architecture. More broadly, our

\*Corresponding Author



Figure 1: Qualitative examples of visual arithmetic. Given a context digit  $x$  and operation  $k$ , the model predicts the target digit  $y = (x + k) \bmod 10$ .

results suggest that the incorporation of appropriate transformation structure into latent transition models may provide a promising direction for representation learning beyond arithmetic domains.

Our contributions are: (1) We introduce MNIST modular arithmetic as a controlled testbed for studying rule learning in latent world models. (2) We show that supervised baselines and JEPAs with additive operation embeddings fit seen operations but fail strict zero-shot extrapolation. (3) We propose BRo-JEPA, a JEPA-style latent dynamics model with an operation-conditioned block-rotation predictor. (4) We demonstrate that BRo-JEPA achieves strong zero-shot and rollout accuracy on unseen modulo-10 operations, and analyze the resulting circular latent geometry.

## 2. Approach

We utilize JEPA [1] to model arithmetic over images. The model predicts the latent representation of a target digit given a context digit image and an arithmetic operation (Fig. 1). We expect this to work because arithmetic operations define consistent transformations between digit states, which can be modeled more naturally in latent space. We propose a novel use of RoPE-like [11] rotation dynamics in a world-modeling setup.

### 2.1. JEPA Model Architecture

We adopt the standard JEPA architecture (Fig. 2) [1]. The context encoder maps the context image to a latent representation, which is concatenated with the operation embedding. The target encoder maps the target image to a latent representation and is updated as an exponential moving average (EMA) of the context encoder. An MLP predictor takes the context–operation latent as input and predicts the target latent. L2 loss is computed between the predicted latent and the target latent. A classifier is attached to the predicted latent, serving as an online probe to quantify the quality of the learned predicted latent representation.

**Additive Compositional Action Embedding** We introduced an additive compositional embedding for actions,

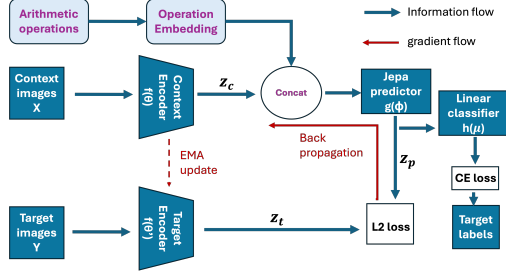


Figure 2: The JEPA architecture of our world model.  $Z_c$ ,  $Z_t$ , and  $Z_p$  represent the context, target, and predicted latent representations respectively.

where each operation  $op(k)$  is represented as a scalar multiple of a learned base vector ( $\mathbf{v}$ ) of the primitive operations (+1 or -1) i.e.  $op(k) = k \cdot \mathbf{v}$ . This parameterization enforces an arithmetic structure by construction, ensuring that relationships such as  $op(+3) = 3 \cdot op(+1)$  hold exactly. This design encodes linear compositionality directly in the embedding space. A list of other embedding methods that we tried is present in Appendix A.1.

**Composition Consistency Loss** To complement the embedding, we introduced a composition consistency loss that explicitly enforces compositional behavior in the predictor. The key idea is that applying the composed operation in one step should match applying its primitive operation sequentially in the predicted latent space. Formally, for the predictor  $g(\phi) = g(z, \mathbf{v})$ , we enforce  $g(z, k \cdot \mathbf{v}) \approx \underbrace{g(g(\dots g(z, \mathbf{v}) \dots), \mathbf{v}))}_{k \text{ times}}$ , where  $z$  is the context latent

representation and  $\mathbf{v}$  is the primitive operations (+1/-1). Because sequentially applying primitive operation has shown great robustness in our rollout evaluation, we can use the sequential rollout predicted latent as the target for our composition consistency loss. Let’s take +2 for an example, where the sequential rollout predicted latent  $z_{seq} = g(g(z, +1), +1)$ , and the direct one-step predicted latent  $z_{direct} = g(z, +2)$ . The composition consistency loss is computed as  $\|z_{direct} - z_{seq}\|^2$  (details in Appx. A.2). This auxiliary objective is not a strict zero-shot setting because it evaluates the predictor at composed operation values during training. We include it as an intermediate baseline to test whether enforcing compositional consistency in an unconstrained predictor is sufficient.

### 2.2. Block Rotation Predictor (BRo-JEPA)

To inject a strong modulo-10 inductive bias of in our model, we propose a novel block-rotation predictor that replaces the standard MLP predictor. The block rotation predictor ensures that the latent representations of various digits are placed in a rotational alignment in high dimensional space. This block rotation is inspired from the Ro-

tary Position Embedding (RoPE) [11]. Unlike standard uses of RoPE as a positional encoding, we use RoPE-inspired rotations as the latent dynamics operator itself. This predictor explicitly preserves the circular structure of the latent space. While an MLP has enough capacity to approximate circular transformations, it is not constrained to learn them. Because an unconstrained MLP can map latent states arbitrarily, it may fit seen operations without preserving the compositional geometry needed for unseen operations. Block rotation addresses this by directly enforcing operation-dependent rotations in latent space. We call the resulting model BRo-JEPA, for Block-Rotation JEPA. BRo-JEPA replaces the unconstrained MLP predictor with an operation-conditioned block rotation in latent space.

Similar to [11], we use a block rotation, where each block is a 2D planar rotation:

$$R(\theta) = \begin{bmatrix} \cos \theta & -\sin \theta \\ \sin \theta & \cos \theta \end{bmatrix}$$

For a  $2n$ -dimensional latent space, the block rotation is:

$$R_{\text{block}} = \begin{bmatrix} R(\theta_1) & 0 & \dots & 0 \\ 0 & R(\theta_2) & \dots & 0 \\ \vdots & \vdots & \ddots & \vdots \\ 0 & 0 & \dots & R(\theta_n) \end{bmatrix}$$

The predictor is a function of the context latent vector  $z$ , operation  $k$ , and rotation  $R_{\text{block}}$ , defined as:

$$g(z, k, R_{\text{block}}(\theta)) = (R_{\text{block}}(\theta))^k \cdot z$$

For each 2D planar rotation we have  $R(\theta)^k = R(k\theta)$ . Thus, we can get the predicted latent  $z_p$  as

$$z_p = R_{\text{block}}(k \cdot \theta) \cdot z$$

The rotation angles  $\theta_i$  can be set as fixed parameters or can also be learnable parameters for our block rotation predictor. In each case, we tested two different strategies: Simple-Frequency Rotation (SFR) and Multi-Frequency Rotation (MFR). In SFR each block (2D plane in the latent space) shares the same rotation angle  $\theta$  while in MFR each block uses its individual  $\theta$ .

For fixed rotation angles, the modulo-10 inductive bias is applied by setting  $\theta = 2\pi/10$  in SFR and  $\theta_i = 2\pi/10 * (i \bmod 5)$  in MFR as illustrated in Appendix Fig. 10.

### 2.3. Representation Collapse Mitigation

JEPA models can exhibit a degenerate solution known as representation collapse [1], where different inputs map to low-variance or indistinguishable latents; we refer to this as latent collapse. This happens in JEPA training when optimization is solely based on the L2 loss between predicted and target latent representations. To mitigate this, several

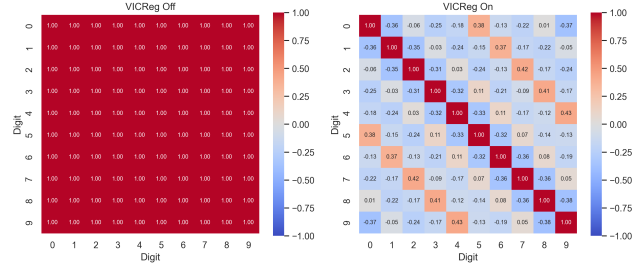


Figure 3: VICReg mitigates latent collapse: without VICReg, all class prototypes collapse to cosine similarity 1; with VICReg, off-diagonal similarities move closer to 0, indicating better-separated prototypes.

strategies have been proposed. Following the JEPA framework, we use a non-gradient target encoder updated as an exponential moving average (EMA) of the context encoder. Additionally, we also use Variance-Invariance-Covariance Regularization (VICReg) [3] that explicitly regularizes the latent space, enforces sufficient feature variance, and reduces redundancy. We adopted VICReg to stabilize training and prevent latent collapse, see Fig 3 (details in Appx. A.3).

### 3. Training Details

We select checkpoints using validation accuracy on held-out context images and seen operations. Zero-shot operation accuracy is reported only once on the held-out test operations. Models were trained in PyTorch for 20 epochs using AdamW with learning rate 0.0001, unless otherwise stated [10, 6].

We train supervised baselines with MLP and ResNet-18 backbones using cross-entropy loss. The MLP baseline takes a flattened MNIST image concatenated with an operation embedding, while the ResNet-18 baseline first encodes the image and then concatenates the resulting feature vector with the operation embedding before classification [5].

For a fair comparison with the JEPA model with block rotation, we added block-rotation to baseline models. The operation-dependent rotation is applied to the last hidden layer of MLP and ResNet-18 encoder features. For MNIST, we adapt torchvision’s ResNet-18 by replacing the initial  $7 \times 7$  convolution with a  $3 \times 3$  stride-1 convolution and removing max pooling. We used the I-JEPA repository and the RoPE repository as references for our implementation.

**Dataset and Setup:** We formulate the task as latent prediction over MNIST, where each image represents a state and arithmetic operations define transitions. Given a context image  $x_{\text{ctx}}$  and an operation  $k \in \{-9, \dots, 9\}$ , the model predicts the latent of the target image  $x_{\text{tgt}}$ . All images are normalized using standard MNIST statistics.

To generate transition pairs, we group images by label

and sample targets using modulo arithmetic. Let  $y_{\text{ctx}} \in \{0, \dots, 9\}$  be the label of  $x_{\text{ctx}}$ , and define  $y_{\text{tgt}} = (y_{\text{ctx}} + k) \bmod 10$ . We then uniformly sample  $x_{\text{tgt}}$  from the subset with label  $y_{\text{tgt}}$ . Context and target images are sampled from the current split (train or test), and  $k$  is sampled uniformly from the split-specific set of operations.

We define *strict zero-shot operation generalization* as evaluation on operation values that are never used in the JEPA prediction loss, classifier loss, or auxiliary losses during training. Unless otherwise stated, models are trained only on operations  $\{-1, +1\}$  and evaluated on unseen operations  $\{\pm 2, \dots, \pm 9\}$ . Models trained with compositional consistency use composed operations in the auxiliary loss and are therefore reported as *weak zero-shot* rather than strict zero-shot.

**Measuring Performance** We evaluate all models primarily using classification accuracy on the MNIST test set, as the dataset is approximately class-balanced. For supervised baselines, accuracy is computed directly from the output logits. For JEPA-based models, accuracy is computed using the probe classifier attached to the predicted latent representation (see Fig. 2).

Table 1 reports train, seen-operation, zero-shot operation, rollout, and latent-space nearest-neighbor accuracies. Seen-operation accuracy uses the MNIST test split with the train operations. Zero-shot accuracy evaluates unseen operations, and nearest-neighbor accuracy checks whether predicted latents are class-discriminative without relying only on the classifier head.

For JEPA models, rollout accuracy measures compositional consistency by repeatedly applying primitive operations in latent space. For example, starting from digit 0, applying  $+1$  five times should produce a latent classified as digit 5. We do not report rollout accuracy for supervised baselines because they output logits directly and do not define iterative latent dynamics.

Finally, we analyze latent structure using class prototypes, computed as the mean latent vector per digit class. Cosine-similarity matrices between these prototypes are used to visualize class separation, as shown in Figs. 3, 7.

## 4. Experiments and Results

We conducted several quantitative and qualitative experiments to evaluate model performance. A summary of our quantitative results are presented in Table 1.

### 4.1. Baseline captures the operation sign but fails to encode the magnitude

From the baseline models as described in Section 3. From Table 1, we see that the models perform exceptionally on seen operations reaching high accuracies of 97.37% and 98.44% for MLP and ResNet-18 variants. However, the zero-shot and unseen operation accuracy maxed to only

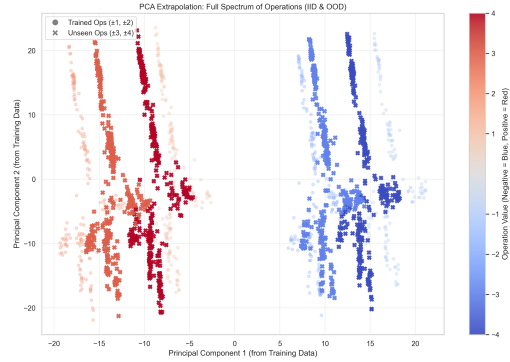


Figure 4: PCA visualization of ResNet baseline latent representation reveals the model captures the sign of operations (red vs. blue) but fails to encode the magnitude (dot vs. cross). Unseen operations ( $\pm 3, \pm 4$ ) arbitrarily crammed in the in-distribution representations ( $\pm 1, \pm 2$ ).

5.92% and 2.42% respectively. This shows that the model fails to generalize even when using additive embedding, which had the extrapolation bias by design.

The Principal Component Analysis (PCA) visualization of the ResNet baseline’s latent space (Figure 4) provides insight into why it fails to generalize to unseen operations. The model partitions its latent representation into operation-specific tracks on the seen operations  $\pm 1, \pm 2$ , forming 4 distinct linear structures (light red and blue). However, when presented with out-of-distribution operations such as  $\pm 3, \pm 4$ , the model correctly predicts the sign of operations but fails to encode the magnitude. As a result, unseen operations are arbitrarily crammed into the in-distribution representation space, leading to extremely poor accuracy. This behavior suggests that baseline lacks the continuous and compositional structural representation required to interpolate or extrapolate the correct target class, resulting in predictive collapse.

### 4.2. JEPA learns symbolic arithmetic operations; fails to extrapolate

Training metrics in Table 1 indicate that the model learned the seen operations effectively: as the training epoch increases, the training loss decreases and the accuracy increases to 98.88% (Fig. 5).

Despite strong performance on seen operations, the model fails to generalize to unseen operations, with high unseen operation test loss and near-zero accuracy (red, Fig. 5). The prototype similarity matrix (right panel, Fig. 5) shows a weak circular structure with similarity decreasing with the distance of digits and again increasing. This suggests that, unlike the baseline model, typical JEPA can capture some compositional and periodic structure in the digits, but the signal is too weak to emerge.

Method	Train Acc.	Seen Op Acc.	Zero-Shot Op Acc.	Unseen Op Rollout Acc.	Unseen Op KNN Acc.
<b>Supervised baselines + additive embedding</b>					
MLP	0.9950	0.9737	0.0593	–	0.0180
ResNet18	0.9989	0.9844	0.0242	–	0.0011
<b>JEPA + additive embedding</b>					
MLP	0.9963	0.9794	0.0995	0.9793	0.1044
MLP w/ compositional consistency loss	0.9928	0.9793	0.9777	0.9786	0.9781
ResNet18	0.9982	<b>0.9946</b>	0.0974	<b>0.9947</b>	0.0903
ResNet18 w/ compositional consistency loss	0.9959	<b>0.9929</b>	<b>0.9931</b>	0.9931	0.7839
<b>Supervised baselines + block rotation on features of encoder</b>					
MLP w/ single-frequency rotation (SFR)	0.9989	0.9773	0.1392	–	0.1422
MLP w/ multi-frequency rotation (MFR)	0.9986	0.9706	0.5650	–	0.5359
ResNet18 w/ single-frequency rotation (SFR)	0.9989	0.9894	0.1010	–	0.1278
ResNet18 w/ multi-frequency rotation (MFR)	0.9991	0.9918	0.5492	–	0.5041
<b>BRo-JEPA</b>					
MLP w/ single-frequency rotation (SFR)	0.9736	0.9431	0.9426	0.9423	0.9428
MLP w/ multi-frequency rotation (MFR)	0.9933	0.9723	0.9724	0.9721	<b>0.9723</b>
ResNet w/ single-frequency rotation (SFR)	0.9915	0.9893	0.9893	0.9893	0.6922
ResNet w/ multi-frequency rotation (MFR)	0.9994	<b>0.9945</b>	<b>0.9946</b>	<b>0.9946</b>	0.7090

Table 1: Ablation over model backbone, compositional consistency loss (c.c. loss) and training objective. The train operations used in this table are just the base operations  $[+1, -1]$ . The test operations are  $[\pm 2, \pm 8]$ . For the block rotations rows the angles are fixed to  $\pi/5$ . Rollout accuracy measures multi-step operation consistency. Fixed angle version of block rotation.

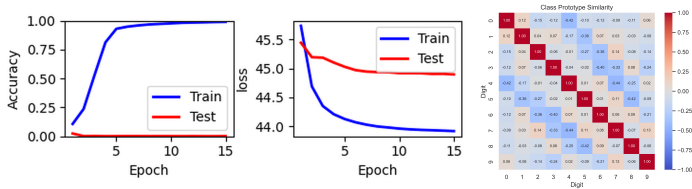


Figure 5: Learning curves show the accuracy and loss during training and test for JEPA model. Class prototype similarity matrix shows the trained target latent cosine similarity for MLP predictor (train op  $\pm 1, \pm 2, \pm 4$  and test ops  $\pm 3$ )

### 4.3. Additive action embeddings do not guarantee zero-shot generalization

The inductive bias in the action embedding ensures the effective compositional dynamics in the embedding space as shown by high rollout accuracy in Table 1. However, direct zero-shot generalization remains unstable: when composed operations, such as  $+3$ , are provided; while the model training operations are only  $\pm 1$ .

The performance initially improves (zero shot accuracy  $\approx 23\%$ ) but later collapses ( $\approx 1-10\%$ ). This suggests that while the embedding encodes the correct structure, the non-linear predictor does not reliably preserve it.

### 4.4. Learned compositional one-step latent dynamics enables rollout arithmetic operations

Both JEPA and its compositional loss variant learns operations such as  $+1$  and  $+2$  successfully, but cannot directly infer compositional equivalence such as  $+2 = +1+1$ , or  $+3 = +1 + 2$ . We hypothesized that the learned one-step primi-

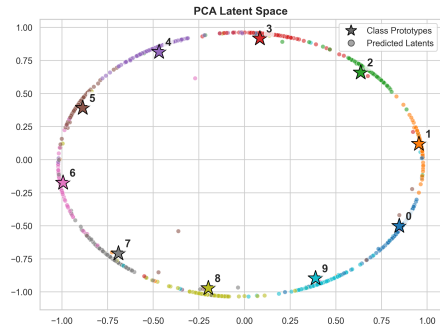


Figure 6: Latent space PCA of SFR block-rotation predictor. By explicitly enforcing rotational dynamics, BRo-JEPA successfully disentangles the latent space into a circular manifold representing the  $\text{mod}(10)$  arithmetic structure.

tive operations ( $+1, -1$ ), can recursively be applied  $n$  times to achieve higher-order operations of  $(+n, -n)$  as a rollout evaluation. The rollout evaluation for  $n$  from 2 to 9 verified our hypothesis and displays its robustness with mean accuracies of  $0.9717 \pm 0.0004$ . Consistent with this, high rollout accuracies are achieved in all versions of JEPA (Table 1).

### 4.5. Fixed Rotation Angles

By applying linear compositional and  $\text{mod}10$  inductive biases in our block rotation predictor using fixed rotation angles, BRo-JEPA achieve zero-shot test accuracies of 94.26% and 98.93% in SFR and 97.24% and 99.46% in MFR for MLP and ResNet encoder respectively (Table 1).

**Geometric Structure of Latent Space in SFR** The PCA of image representations shows that block rotation suc-

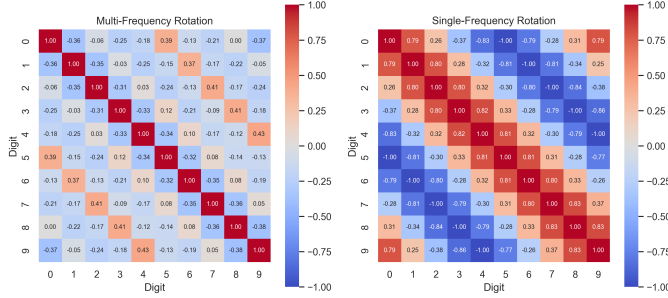


Figure 7: Class prototype cosine-similarity matrices for MFR and SFR block-rotation JEPAs.

cessfully coerces the latent space into a continuous elliptical manifold in SFR (Figure 6). The class prototypes arrange themselves sequentially on the circle. This geometric configuration demonstrates that the model internalized the modular arithmetic topology that corresponds latent rotation to arithmetic operations.

In the SFR latent space, the fixed rotation angle  $\theta = 2\pi/10$  induces a circular modulo-10 structure. Therefore, digit pairs five steps apart, such as 0/5, 1/6, 2/7, 3/8, and 4/9, become approximately antipodal because applying  $+5$  corresponds to a rotation by  $\pi$ . This explains the near  $-1$  cosine similarity for these pairs in Fig. 7. Pairs four or six steps apart, such as 0/4 or 1/5, also show strong negative similarity because their angular separation is close to, but not exactly,  $\pi$ . In PCA, these negatively correlated prototypes appear on opposite sides of the elliptical manifold, reflecting the learned modulo-10 geometry. The corresponding MFR PCA visualization is shown in Appendix Fig. 13.

In Fig. 7, MFR has off-diagonal similarities closer to zero than SFR, showing that its class prototypes are more decorrelated and better separated. While SFR uses one rotation frequency and creates strong periodic correlations, MFR spreads the modulo-10 structure across multiple frequencies. This prevents any single circular pattern from dominating the similarity matrix and gives a more balanced latent space. MFR’s higher accuracy (Table 1) confirms that multi-frequency rotations better capture underlying structure and improve robustness to dataset variability.

PCA (Figure 6) shows the circular latent manifold; multi-step rollouts test its stability by repeatedly applying an operation from digit 0. The  $-3$  trajectory (Fig. 8) highlights the model’s extrapolation and compositional characteristics. Although the model was trained only on  $\pm 1$ , it follows the correct zero-shot sequence  $0 \rightarrow 7 \rightarrow 4 \dots$  when given the  $-3$  operation. Low drift suggests that the predictor learned the modular arithmetic rule rather than memorizing local transitions. More trajectories are in Appx. Fig. 14.

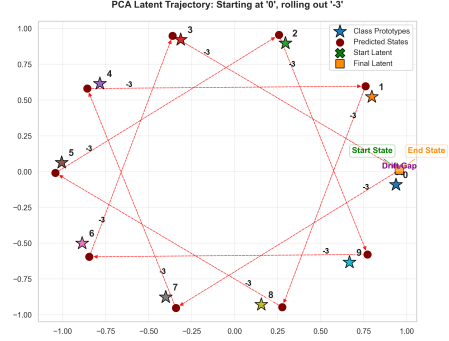


Figure 8: PCA visualization of multi-step latent trajectories for the SFR block-rotation predictor under the zero-shot operation  $-3$ . Starting from digit 0, the model composes unseen operations with no drift across rollout steps.

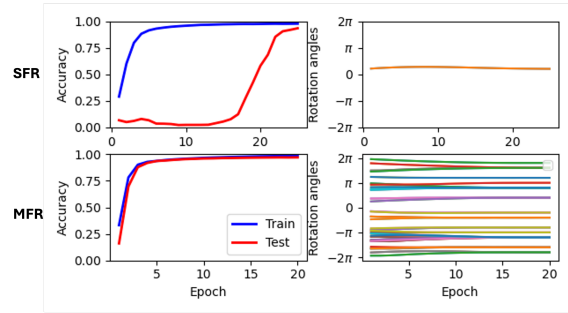


Figure 9: Learning curves show the accuracy (left) and rotation angles (right) during training for SFR and MFR

#### 4.6. Learnable Rotation Angles

In both SFR and MFR the predictor successfully learns the rotation angles when  $\theta$ s are learnable parameters, converging rapidly during training to accuracies of 0.9767 and 0.9742 accordingly (blue, Fig.9). However, generalization to unseen operations differs remarkably (red curves). In MFR, testing accuracy quickly matches the training performance with similar trajectory, achieving 0.9711. In contrast, SFR exhibits a significant delay: the testing accuracy remains near 0 for many epochs then gradually reaches 0.9334, way below the training performance. This indicates while SFR learns representations to fit the training data but fails to generalize early on, MFR facilitates learning of effectively-generalized representations at the outset.

Starting from random initialization in the range of  $[-2\pi, 2\pi]$ , the learned rotation angles converge to discrete values corresponding to  $\pi/5$  and its harmonics as shown in Fig. 9 (right). In SFR, the shared rotation angle  $\theta$  converges to  $\pi/5$  (left), aligned with that in our fixed rotation angles. In MFR, the 32 learned rotation angles converge to a set of distinct harmonic components of  $\pi/5$ , with 13 unique ones observed here.

The specific harmonic component to which each rotation angle converges depends on the initial conditions. It seems that the current JEPA model objective exhibits multiple local minima corresponding to these harmonic solutions. As a result, the learned rotation angles tend to be trapped in one of these minima. This behavior affects MFR little due to the presence of multiple independent rotation angles, but it significantly degrades the performance in SFR when the learned angle converges to a higher order harmonic of  $\pi/5$  instead of the fundamental frequency itself (see Appx. A.4).

BRO-JEPA captures the modulo-10 structure in the data by leveraging a compositional inductive bias in the latent space under both SFR and MFR. By allowing independent rotation angles, MFR learns a Fourier-like decomposition of transformations, where different latent pairs encode different frequency components of the modulo-10 dynamics. This suggests that the learned latent dynamics distribute modular structure across multiple frequency components rather than relying on a single global rotation, which helps explain MFR’s faster convergence and stronger generalization to unseen operations.

#### 4.7. Zero Shot Performance on Unseen Operations

Although compositional consistency loss achieves very high zero-shot accuracy of 99.31% (Table 1), it is not strictly zero-shot, as the predictor indirectly exposes to unseen operations via the training objective. We therefore consider this weak zero-shot result.

The block-rotation predictor is zero-shot in operations, as all unseen operations are inferred via the rotational structure learned in the latent space, and the model never sees operations beyond training set. Its 99.46% zero-shot accuracy demonstrates that JEPA with block-rotation predictor learned in its latent representation a compositional structure that enables unseen arithmetic operations.

### 5. Limitations

Our experiments are conducted on MNIST modular arithmetic, a highly controlled setting with a known cyclic group structure. The block-rotation predictor explicitly matches this structure, so the results do not imply that the same architecture will generalize to arbitrary symbolic reasoning tasks. In addition, our strongest results rely on fixed or learnable rotational inductive biases that encode the periodicity of modulo-10 arithmetic. Future work should test whether similar structured latent dynamics can be learned in less controlled visual domains, larger state spaces, and tasks where the underlying transformation group is unknown.

### 6. Conclusion

Our results support the main hypothesis. JEPA learned arithmetic transformations structures in latent space while

supervised baselines couldn’t. Additive operation embeddings and compositional consistency loss alone did not generalize to strict zero-shot operations. BRO-JEPA addressed this by imposing the modulo-10 structure directly in latent space. With this inductive bias, the model achieved high seen-operation, truly zero-shot, rollout, and KNN accuracy, suggesting that the latent transition dynamics captured compositional structure beyond just the training distribution.

### References

- [1] Mahmoud Assran, Quentin Duval, Ishan Misra, Piotr Bojanowski, Pascal Vincent, Michael Rabbat, Yann LeCun, and Nicolas Ballas. Self-supervised learning from images with a joint-embedding predictive architecture. In *Proceedings of the IEEE/CVF conference on computer vision and pattern recognition*, pages 15619–15629, 2023. 1, 2, 3
- [2] Mahmoud Assran et al. V-jepa 2: Self-supervised video models enable understanding, prediction and planning. *arXiv preprint arXiv:2506.09985*, 2025. 1
- [3] Adrien Bardes, Jean Ponce, and Yann LeCun. Vi-creg: Variance-invariance-covariance regularization for self-supervised learning. *arXiv preprint arXiv:2105.04906*, 2021. 3
- [4] Li Deng. The mnist database of handwritten digit images for machine learning research [best of the web]. *IEEE Signal Processing Magazine*, 29(6):141–142, 2012. 1
- [5] Kaiming He, Xiangyu Zhang, Shaoqing Ren, and Jian Sun. Deep residual learning for image recognition. In *Proceedings of the IEEE conference on computer vision and pattern recognition*, pages 770–778, 2016. 3
- [6] Ilya Loshchilov and Frank Hutter. Decoupled weight decay regularization. In *International Conference on Learning Representations*, 2019. 3
- [7] Andreas Madsen and Alexander Rosenberg Johansen. Neural arithmetic units. In *International Conference on Learning Representations*, 2020. 1
- [8] Bhumika Mistry, Katayoun Farrahi, and Jonathon Hare. A primer for neural arithmetic logic modules. *Journal of Machine Learning Research*, 23(185):1–58, 2022. 1
- [9] Nature Editorial. ‘World models’ are AI’s latest sensation: what are they and what can they do? *Nature*, apr 2026. 1
- [10] Adam Paszke, Sam Gross, Francisco Massa, Adam Lerer, James Bradbury, Gregory Chanan, Trevor Killeen, Zeming Lin, Natalia Gimelshein, Luca Antiga, et al. Pytorch: An imperative style, high-performance deep learning library. *Advances in neural information processing systems*, 32, 2019. 3
- [11] Jianlin Su, Yu Lu, Shengfeng Pan, Bo Wen, and Yunfeng Liu. Roformer: Enhanced transformer with rotary position embedding, 2021. 2, 3
- [12] Alberto Testolin. Can neural networks do arithmetic? a survey on the elementary numerical skills of state-of-the-art deep learning models. *Applied Sciences*, 14(2):744, 2024. 1
- [13] Andrew Trask, Felix Hill, Scott E Reed, Jack Rae, Chris Dyer, and Phil Blunsom. Neural arithmetic logic units. *Advances in neural information processing systems*, 31, 2018. 1

## A. Appendix

### A.1. Operation Embeddings

We explored several ways of encoding the arithmetic operation as an input feature. The goal was to represent the operator in a form that the model can use for either memorization of seen operations or generalization to unseen ones.

- **Lookup embedding:** Each discrete operation is assigned a learned vector from an embedding table. This is the simplest option and works well when the set of operations is fixed and known in advance, but it does not naturally generalize to unseen values.
- **Linear embedding:** The raw scalar operation value is projected through a small neural network. This gives a continuous representation that can handle arbitrary operation values and is more flexible than a lookup table.
- **Fourier embedding:** The operation value is mapped to sinusoidal features such as  $\sin(x)$ ,  $\cos(x)$ ,  $\sin(2x)$ ,  $\cos(2x)$  before projection. This encodes periodic structure and tends to support smoother generalization across nearby operations.
- **Hybrid embedding:** The sign of the operation and its magnitude are encoded separately. The sign is handled with a categorical embedding, while the magnitude is represented with Fourier features. This aims to capture both operator direction and numeric scale.

### A.2. Training process for composition consistency loss

$z_{seq}(n * \text{primitive operation})$  is computed by recursively applying the primitive operation to the model  $n$  times, while  $z_{direct}(n * \text{primitive operation})$  is computed by directly applying the high order operation  $n * \text{primitive operation}$  in one step.

In practice, we find the smallest positive training op and smallest negative training op: +1 and -1 in the compositionality setup. Then for each requested composition op, for example 4 or -4,  $z_{seq}$  is computed by applying the primitive operation 1 or -1 recursively 4 times.  $z_{direct}$  is computed by applying 4 or -4 to the JEPa model directly. The composition consistency loss is calculated as  $|z_{seq} - z_{direct}|^2$ , which is added to the regular JEPa loss with a weight hyperparameter.

### A.3. Variance-Invariance-Covariance Regularization (VICReg)

The model optimizes the objective  $\mathcal{L} = \lambda\mathcal{L}_{inv} + \mu\mathcal{L}_{var} + \nu\mathcal{L}_{cov}$  to prevent latent collapse. The L2 invariance loss

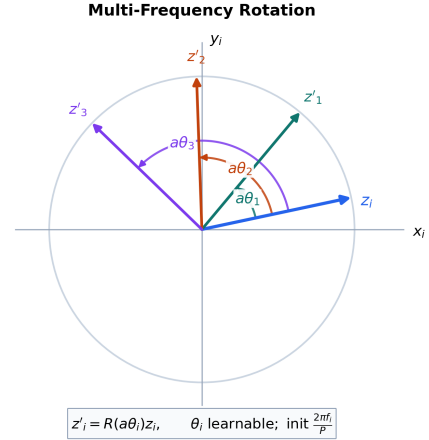


Figure 10: Working of multi-frequency rotation, each pair of  $z$  is rotated by different angles. In the case of SFR, each  $\theta_i$  is same.

( $\mathcal{L}_{inv}$ ) aligns the predicted and target latents, i.e., the standard JEPa loss. The variance loss ( $\mathcal{L}_{var}$ ) is a hinge loss that incentivizes the standard deviation of each latent dimension across the batch to be above a certain threshold (1 in this work). The covariance loss ( $\mathcal{L}_{cov}$ ) minimizes the covariance between each pair of latent dimensions across the batch. In this way, VICReg prevents representations of different samples in a batch (including those from different classes) from collapsing to the same trivial invariant features, thereby avoiding latent collapse.

For VICReg to work, a relatively large batch size is required. For all experiments, we use a batch size of 128. We use the default parameter values from the original VICReg paper:  $\lambda = 25$ ,  $\mu = 25$ ,  $\nu = 1$ .

### A.4. SFR degrades in learnable rotation angles

With a different initial condition of  $\theta$ s ( $\in [0, 2\pi]$ ), MFR still learns robustly with both 97% accuracy in both training and testing, while SFR significantly degrades its performance in both settings. (Fig. 11). Correspondingly,  $\theta$  in SFR converges to a higher-order harmonics  $8\pi/5$  instead of the base frequency  $\pi/5$  (Fig. 12, left), which breaks the compositional modulo-10 structure in the latent space needed for arithmetic operation. MFR on the other hand, shows the flexibility in learning with multiple independent frequencies (Fig. 12, right).

### A.5. Geometric Structure of Latent Space

The +1 trajectory in Figure 14a demonstrates the model’s recurrent stability. Despite relying on purely its own predictions for 10 sequential gaps, the model accurately visits every class prototype with minimal drift upon returning to the start state. This demonstrates the block ro-

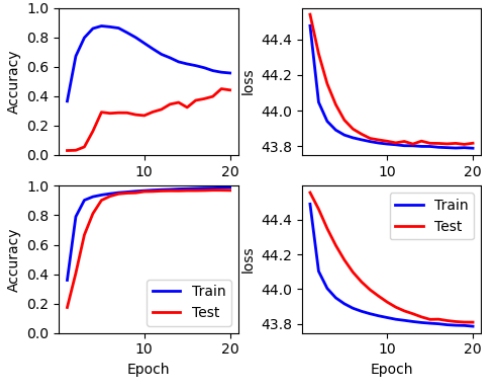


Figure 11: Learning curves show the accuracy (left) and loss (right) during training (blue) and test (red) for single-frequency rotation (top) and multi-frequency rotation (bottom)

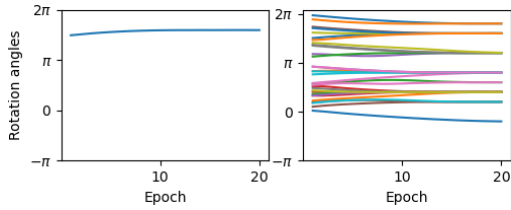


Figure 12: Learning curves show the accuracy (left) and loss (right) during training (blue) and test (red) for single-frequency rotation (top) and multi-frequency rotation (bottom)

tation operator applies rigid transformations without compounding error.

### A.6. Multi-Frequency Rotation - PCA Plots

In the MFR PCA visualization, digit pairs separated by five modular steps, such as 0/5, 1/6, 2/7, 3/8, and 4/9, appear close in the two-dimensional projection. This does not necessarily indicate latent collapse. Since MFR uses multiple rotation frequencies, the +5 transformation affects different latent blocks differently: some frequency components make these pairs antipodal, while others make them similar. PCA shows only the dominant two directions of variance, so it can group these half-cycle pairs together even when they remain separable in the full latent space. Consistent with this, the MFR heatmap in Fig. 7 shows only moderate similarity for these pairs rather than near-perfect correlation, indicating that class information is still distributed across the remaining latent dimensions.

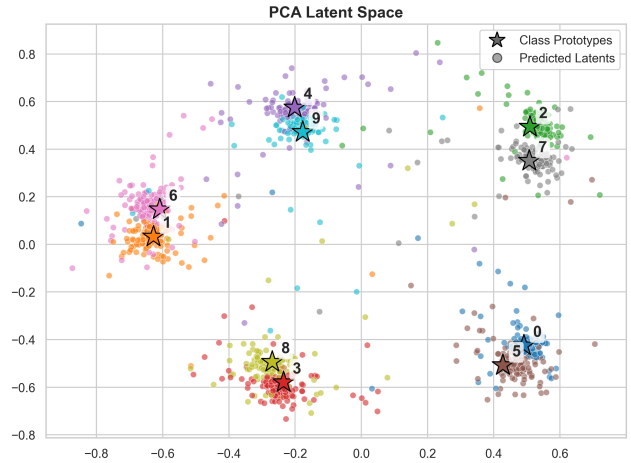
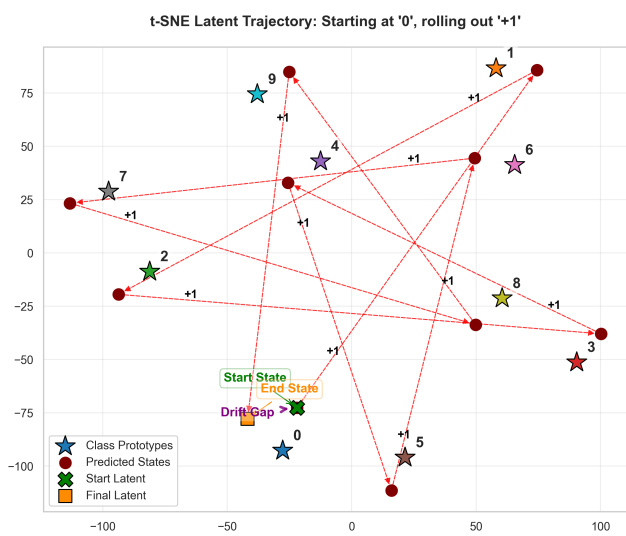
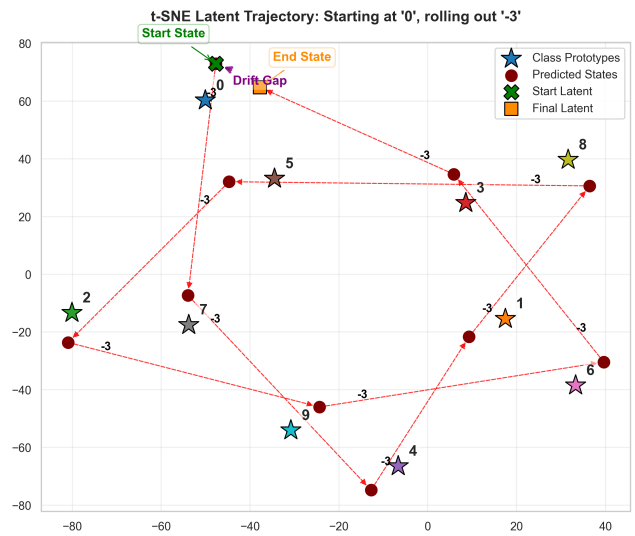


Figure 13: Latent space PCA of MFR block-rotation predictor. By explicitly enforcing rotational dynamics, the model successfully disentangles the latent space into a circular manifold representing the  $mod(10)$  arithmetic structure.



(a) Rollout for +1 (In-Distribution)



(b) Rollout for -3 (Zero-Shot)

Figure 14: t-SNE visualization of multi-step latent trajectories for the Block Rotation predictor (MFR). Starting from an initial state of 0, the model demonstrates high stability over 10 sequential steps for trained operations (a) and successfully composes unseen operations with a minimal drift gap (b).